Article

Visualization of Sliding and Deformation of Orbital Fat During Eye Rotation

Gijsbert J. Hötte[1,*,✉], **Peter J. Schaafsma**[2,*,✉], **Charl P. Botha**[2,3 ✉],
Piotr A. Wielopolski[4 ✉], and **Huibert J. Simonsz**[1 ✉]

[1] Department of Ophthalmology, Erasmus Medical Center, Rotterdam, the Netherlands
[2] Department of Mediamatics, Technical University Delft, Delft, the Netherlands
[3] Department of Radiology, Laboratory for Clinical and Experimental Image Processing, Leiden University Medical Center, Leiden, the Netherlands
[4] Department of Radiology, Erasmus Medical Center, Rotterdam, the Netherlands

Correspondence: Gijsbert J. Hötte, Department of Ophthalmology, room Ba-108 Erasmus Medical Center, PO Box 2040, 3000 CA Rotterdam, the Netherlands. e-mail: g.j.hotte@erasmusmc.nl

Purpose: Little is known about the way orbital fat slides and/or deforms during eye movements. We compared two deformation algorithms from a sequence of MRI volumes to visualize this complex behavior.

Methods: Time-dependent deformation data were derived from motion-MRI volumes using Lucas and Kanade Optical Flow (LK3D) and nonrigid registration (B-splines) deformation algorithms. We compared how these two algorithms performed regarding sliding and deformation in three critical areas: the sclera-fat interface, how the optic nerve moves through the fat, and how the fat is squeezed out under the tendon of a relaxing rectus muscle. The efficacy was validated using identified tissue markers such as the lens and blood vessels in the fat.

Results: Fat immediately behind the eye followed eye rotation by approximately one-half. This was best visualized using the B-splines technique as it showed less ripping of tissue and less distortion. Orbital fat flowed around the optic nerve during eye rotation. In this case, LK3D provided better visualization as it allowed orbital fat tissue to split. The resolution was insufficient to visualize fat being squeezed out between tendon and sclera.

Conclusion: B-splines performs better in tracking structures such as the lens, while LK3D allows fat tissue to split as should happen as the optic nerve slides through the fat. Orbital fat follows eye rotation by one-half and flows around the optic nerve during eye rotation.

Translational Relevance: Visualizing orbital fat deformation and sliding offers the opportunity to accurately locate a region of cicatrization and permit an individualized surgical plan.

Introduction

Orbital fat is the tissue inside the orbit in which other orbital structures, such as the eyeball, optic nerve, and eye muscles, are embedded. It consists of a mesh of small compartments that each contain a large number of fat cells. These compartments can deform, but the structure they form remains intact. The fat cells are larger just behind the eyeball, and smaller near the lateral and medial orbital walls. Possibly, this is related to the steepness of the local average pressure gradient, with cells being larger in lower gradient regions.[1]

The eye is pulled backward by four of the extraocular muscles. The fat is divided by septa and in part by intermuscular membranes. In most present models of ocular motility three degrees of freedom in eye rotation are permitted. In these models it is assumed that the eye rotates about a single point, which coincides with the center of the globe. Obviously, when four rectus muscles together pull the eye backward, without a force acting in the opposite direction, such a model cannot be comprehensive.

When using a model with six degrees of freedom, however, the muscles would pull on the globe,

whereas the reactive force, exerted by the orbital fat, would push it in the opposite direction. To obtain a comprehensive model of eye rotation within the orbit, finite element models have been constructed. The orbital fat is difficult to model as it deforms and slides excessively. Hence, the elements, for instance tetraeders that represent the fat, are deformed to an extent that algorithm errors occur and the model crashes on strong eye rotation.

Schoemaker et al.[2] previously reported in a MRI study, which was registered by hand, that fat immediately behind the eye follows eye rotation by approximately one-half. To this day however, it is unknown what happens with the optic nerve during eye rotation: the eye slides within Tenon's capsule but the optic nerve is attached to the eye, and therefore, in one way or the other, it sloshes through the fat as the eye rotates at high speeds during saccades. Moreover, what happens with the fat between muscle and sclera when the muscle is rolled onto the globe as the eye rotates? Is it squeezed out sideways, or does the fat slide backward?

In the model developed by Schoemaker, sliding of fat was measured by the amount of displacement of tissue markers such as blood vessels.[2] Instead of using markers to estimate the amount of displacement, a vector field-based calculation could provide a reasonably accurate representation. Also, the vector displacement could be well visualized in three-dimensions (3D). Abràmoff et al.[7,8] compared four different optical flow methods by Fleet and Jepson,[3] Uras et al.,[4] Singh,[5] and Lucas and Kanade[6] (LK3D) for the calculation of deformation data from static MRI volumes. They concluded that the latter gave the best result for MRI imaging of the eye rotation in the orbit.[7,8]

Optical flow methods such as LK3D result in a sequence of deformation velocity fields, where each vector estimates the direction and degree at which a local patch of tissue is deforming at a specific instant.[9] Recently, however, a ready-to-use deformation calculation package has been described, called B-splines mutual information nonrigid registration (B-splines).[10] This method uses nonrigid registration to calculate deformation within a dataset of volumes and, like other registration methods, results in deformation-offset fields.[11,12]

Botha et al.[13] used fixed-region deformation queries to show how a small spherical region of soft tissue deforms over time. Direct visualization of dense deformation data in a pair of time-spaced volumes was investigated by Busking et al.[14] Piccirelli et al.,[15,16] as well as, Prince and McVeigh[17] used two-dimensional (2D)-tagged MRI to directly track and visualize the internal deformation of soft tissue, specifically muscles, in the orbit. Controlling and understanding these visualizations is problematic for clinicians, anatomists, and other experts. Also, a proper representation of the deformation and sliding patterns provides a solid foundation for further finite element modelling. Therefore, obstacles need to be overcome to improve the current techniques for visualization of deformation of the fat.

In this paper, we compare two previously described deformation calculation methods from a sequence of MRI volumes (LK3D and B-splines) in a pipeline for the multiscale, dynamic, explorative visualization of orbital fat sliding and deformation. Subsequently, we investigate which of the two methods allows better visualization, and therefore better understanding, of three clinically relevant questions: (1) to what extent the fat moves with the eye during eye rotation, (2) how the optic nerve moves through the fat during eye rotation, and (3) to what extent fat is squeezed out under the tendon of the eye muscles during eye rotation.

Materials and Methods

Description of the Visualization Pipeline

MRI Acquisition

The previously described T1 MRI scans[13] were made of a healthy 22-year-old male volunteer (after informed consent and in accordance with the declaration of Helsinki) on a General Electric 3.0T Signa Excite 3 MRI scanner (GE Healthcare, Wautwatosa, WI) at Erasmus Medical Center (Rotterdam, the Netherlands) using the transmit body coil for signal excitation and a dedicated 4-channel dual array receive only surface coil (2 channels per eye; Flick Engineering Solutions BV, Winterswijk, NL) for signal reception to enhance signal quality. Imaging was performed using a 3D fast spoiled radio frequency gradient echo scan (SPGR) with a repetition time (TR) of 6.03 ms, echo time (TE) of 2.1 ms, and a readout flip angle of 10°. The scanning field-of-view (FOV) was set to 140 mm using an acquisition matrix of 170×170 and 62, 1-mm axial slices encoded, resulting in an actual voxel resolution was $0.823 \times 0.823 \times 1.000$ mm^3 (coronal $\times$ sagittal $\times$ axial) in a total acquisition time per 3D volume of 1 minute 0 seconds. The receiver readout bandwidth was set to 62.5 KHz and no imaging acceleration techniques nor

surface intensity correction algorithms were used. The resulting dataset was interpolated by zero-filling before the fast Fourier transform to an interpolated voxel size of $0.5469 \times 0.5469 \times 0.5000$ mm^3 providing a grid of $256 \times 256 \times 116$ voxels that was used for further processing. Each scan was acquired with a different axial angle of rotation for the right eyeball, which abducts from $-30°$ (left) of rotation to $+40°$ (right) at constant $5°$ increments. To minimize vergence, the subject's left eye was covered. The angle of rotation was imposed by requiring the subject to focus on a small light source placed 20 cm from the center of the right eyeball. To minimize acquisition errors due to head movement during or between scans, two previously described measures (Dunning AG, et al., *IOVS* 2009;50:ARVO E-Abstract 661) were, taken. First, the subject's head was fixed inside a frame to minimize head movement during each scan. Second, the subject bit down on a dental thermoplast with 3D MRI markers for rigid registration of the volumes afterward. With this set up, only in the $45°$-gaze positions in extreme left and right gaze, any head movement occurred. We obtained a sequence of 15 axial MRI slabs of a healthy male subject (Fig. 1, 1a), containing both orbits. Because the acquisition focus was on the right orbit, we cropped the dataset to fully contain only the right eye socket. The size of the cropped grid is $61 \times 96 \times 86$ voxels. The volumes of the acquired MRI data together represent the gradually sliding and deforming anatomy of the orbital fat in a motion-MRI (Video 1).

Deformation Calculation and Visualization

As shown in Figure 1, and described in detail in Appendix A, the pipeline consists of three phases: (1) data acquisition and processing, (2) specification of a region of interest (ROI), and (3) marker-based deformation visualization.

As long as the result of the acquisition is a sequence of MRI volumes representing the gradually deforming anatomy (Fig. 1, 1a; Video 1), a variety of deformation calculation algorithms can be applied to the MRI sequence to obtain an estimate of this deformation (Fig. 1, 1b). To express errors in the deformation data, due to MRI noise or flaws in the algorithm, a deformation uncertainty measure is calculated (Fig. 1, 1c).

Initially, only a surface showing prominent anatomical features is visible. In the second phase, however, the user selects a ROI (i.e., a subregion of the complete anatomy for current visual inspection).

The user positions a plane through the anatomy using this initial surface as a frame of reference (Fig. 1, 2a). After adjusting or fine-tuning its position (Fig. 1, 2b), he draws an outline on the plane. He then extrudes this outline to define the intended 3D subregion (i.e., the ROI; Fig. 1, 2c).

In the third phase, the calculated deformation was visualized by showing a smooth animation of tissue motion. Numerous small dots, called markers, are placed inside the ROI (Fig. 1, 3a). Each marker is colored according to its current uncertainty value, and shaped according to the instantaneous degree of deformation at the marker's position (Fig. 1, 3b). Immediately, the markers begin moving according to the deformation data, creating a detailed impression of deforming tissue (Fig. 1, 3c). The anatomical surface, the plane and marker appearance are constantly updated to reflect the current anatomy, tissue deformation, and deformation uncertainty.

As mentioned, two different deformation calculation methods were used. Further in-depth analysis of the two methods is outlined in Appendix B, whereas a more detailed description of the pipeline can be found in Appendix A.

Clinical Application

Next, we investigated the application of the presented pipeline in three clinically relevant areas in the human orbit. Precise descriptions of the ROI placement can be found in Appendix A.

Sliding and Deformation of Orbital Fat Near the Eyeball

First, we investigated to what extent the rotating eyeball slides over the retrobulbar fat and to what extent the fat moves with the eye during eye rotation. Described by Schoemaker et al.,[2] the orbital fat immediately behind the eyeball follows the displacement of the eyeball surface during rotation by approximately one-half. In this experiment, we tried to verify that result.

Sliding and Deformation of Orbital Fat Around the Optic Nerve

Secondly, we examined the sliding and deformation patterns of the orbital fat around the optic nerve during abduction: in front of the optic nerve, behind the optic nerve, and alongside the optic nerve.

Displacement of Orbital Fat Between Eyeball and Medial and Lateral Rectus Muscles During Abduction

Next, we investigated fat motion in the region between the eyeball and the rectus muscles. During
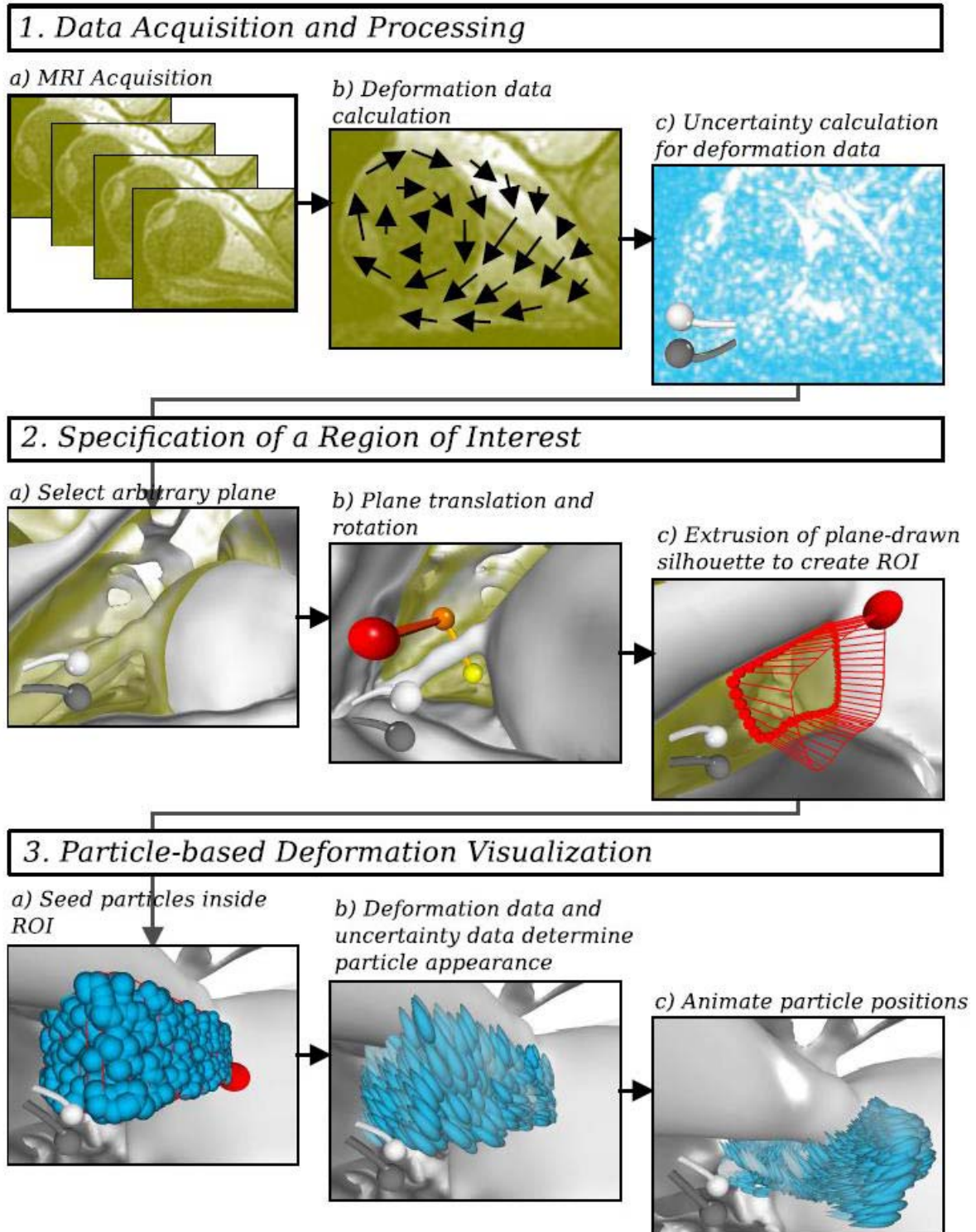
Figure 1. Visualization pipeline. The figure shows a pipeline for the visualization of the deformation of soft tissue in the human body. It consists of three phases: (1) data acquisition and processing, (2) specification of a ROI, and (3) marker-based deformation visualization. The first phase is a preprocessing phase, while the second and third phases are implemented in an interactive visualization application, controlled by the user, and between which he can frequently switch. Phase 1 (*top*): during the first phase, MRI data of the deforming anatomy is acquired. As long as the result of the acquisition is a sequence of MRI volumes representing the gradually deforming anatomy (1a), a variety of algorithms can be applied to the MRI sequence to obtain an estimate of this deformation (1b). To express errors in the

deformation data, due to MRI noise or flaws in the algorithm, a deformation uncertainty measure is calculated (1c), to be used during visualization. Phase 2 (*middle*): in the second phase, the user selects a ROI, (i.e., a subregion of the complete anatomy for current visual inspection). Initially, only a surface showing prominent anatomical features is visible. The user positions a plane through the anatomy using this surface as a frame of reference (2a). After adjusting or fine tuning its position (2b), he draws on the plane an outline. He then extrudes this outline to define the intended subregion (i.e., the ROI; 2c). Phase 3 (*bottom*): In the third phase, deformation is visualized by showing a smooth animation of tissue motion. Numerous small dots, called markers, are placed inside the ROI (3a). Each marker is colored according to its current uncertainty value, and shaped according to the instantaneous degree of deformation at the marker's position (3b). Immediately, the markers begin moving according to the deformation data, creating a detailed impression of deforming tissue (3c). The anatomical surface, the plane, and marker appearance are constantly updated to reflect the current anatomy, tissue deformation, and deformation uncertainty.

abduction, the lateral rectus muscle rolls up onto the eyeball. This would cause orbital fat to be pushed backward or sideways from between eyeball and muscle. An observable effect of this behavior would be that a volume of markers in this region between muscle and eyeball would get stretched in the direction of the eyeball rotation axis. Also during abduction, we expected the lateral muscle to roll off from the eyeball and some fat to move from above and below.

Validation Experiments

The tool was validated by using the deformation data to predict the shape and location of three ROIs: one for which we know the deformation data, and two for which we can estimate the deformation by identifying the demarcated regions in other MRI volumes later in the acquisition sequence. This gives us a subjective estimate of the reliability of the methods for MRI data.

First, we examined a synthetic dataset, consisting of a single MRI volume that is uniformly translating in 3D world space in one direction of which no deviation of the original grid structure is to be expected. The other experiments involved tracking of the eye lens in the eye and a section of blood vessels in the fat, respectively.

Results

Visualization Pipeline

The volumes of the acquired MRI data together represent the gradually sliding and deforming anatomy of the orbital fat in a motion-MRI (Video 1). Deformation and sliding patterns of the orbital fat were visualized in a clear and ordered fashion of the section deemed interesting. Presence of noise or lack of spatial resolution limited detection of small

anatomical features, and consequently their contribution to the deformation data.

Clinical Application

Sliding and Deformation of Orbital Fat Near the Eyeball

In Figure 2 (right), we see how markers generally move in the direction of rotation of the eyeball. As evidenced by the shape and position of the marker's mass, the fat at the sclera-fat interface moved approximately one-half the distance the surface of the eyeball moved. It should be emphasized that in fact this comprises a combination of simultaneous sliding and deformation. Also, the effect of the rotating eyeball on fat displacement decreased with its distance to the eyeball.

Sliding and Deformation of Orbital Fat Around the Optic Nerve

We expected to see the orbital fat being pushed away to the side in front of the optic nerve, and behind it to see orbital fat partially moving with the optic nerve and also some displacement of orbital fat into the path of the optic nerve.[2] In Figure 3, we see these deformation patterns are indeed observed when using LK3D, allowing the fat tissue to be disrupted as a more rigid structure (i.e., the optic nerve) slides through it.

The sliding-through behavior of the optic nerve was also observed in its wake (Fig. 4). The figure shows deformation in this area using three different marker configuration styles. We see in the top panel, a randomly distributed ROI, that the volume near the optic nerve is elongated and thinned in its direction of motion, while the region nearer to the lateral rectus muscle stays more in place, but is spread sideways. This pattern is confirmed in the bottom-right panel, which shows deformation of a vertical sheet of tissue over a significantly shorter time than the first panel. From the left edge of the ROI, it is clear that the top
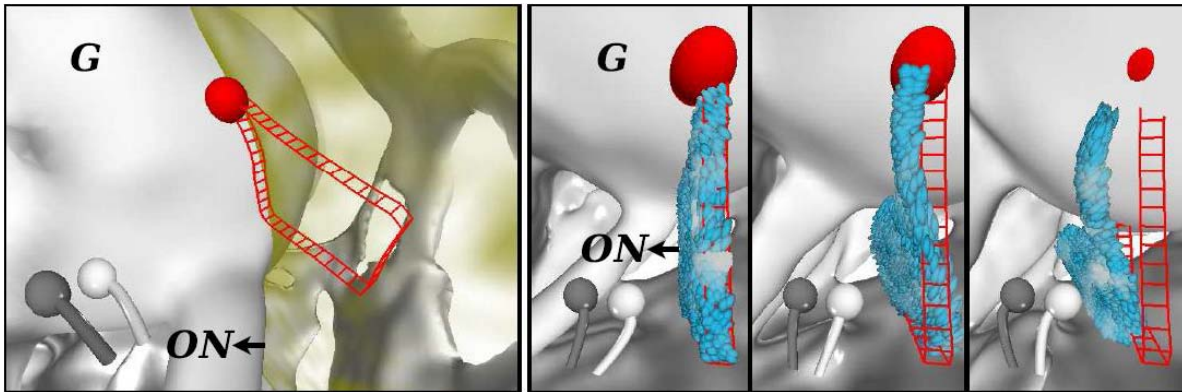
Figure 2. Deformation and sliding near the eyeball (B-Splines). *Left*: a slim ROI is created superior to the right optic nerve. *Right*: superior view of the ROI and moving markers at −35°, 0°, and +35° of rotation. When compared with the displacement of the attachment point of the optic nerve, markers right next to the eyeball seem to move approximately one-half that amount. Marker displacement decreases with distance from the eyeball.

half of the grid-configuration sheet changes little shape, but the bottom half (nearer to the optic nerve) is growing thinner and is stretched along the optic nerve's path. The bottom-left panel shows a peculiar deformation pattern. A sheet of markers near the optic nerve curls in on itself, appearing to enclose a region that is dragged along with the optic nerve, and indicating that tissue to the side of the optic nerve moves significantly slower along with it than tissue right behind and in front of it.
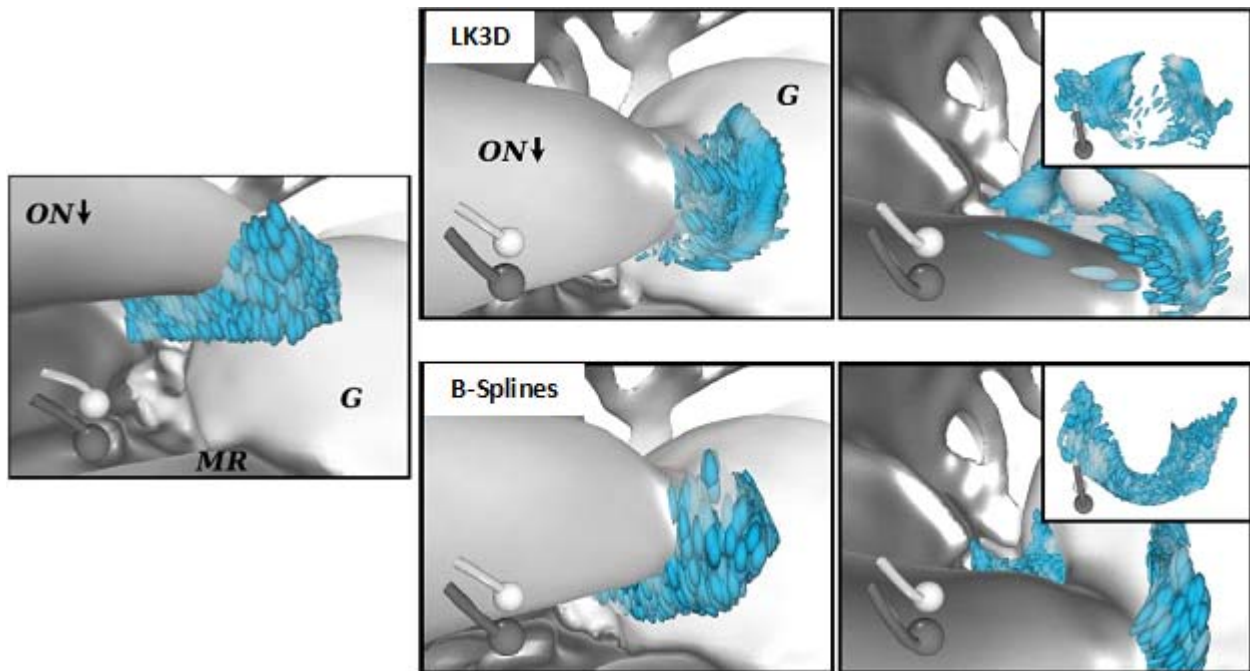
Figure 3. Deformation in front of the optic nerve. *Left*: ROI just in front of the optic nerve is filled with droplet markers. Eye ball rotation is at −40°. *Center*: at −10°, marker positions indicate that tissue has been moving along with the optic nerve. Right in front of the optic nerve, tissue deformation matches displacement of the optic nerve, while to its sides, tissue moves along with it only partially. At this stage, no significant difference with LK3D is yet observed. *Right*: final deformation at +25°. *Insets* show an overview of the deformation. At this stage LK3D shows a separation between superior and inferior soft tissue regions is observed, consistent with the liquid-like properties of the eye fat. B-splines on the other hand shows lack of convergence of the eye fat behind the optic nerve. The *inset* confirms this, and also shows that tissue remains connected, while it is expected that regions of orbital fat can freely be disconnected where more rigid structures approach each other.
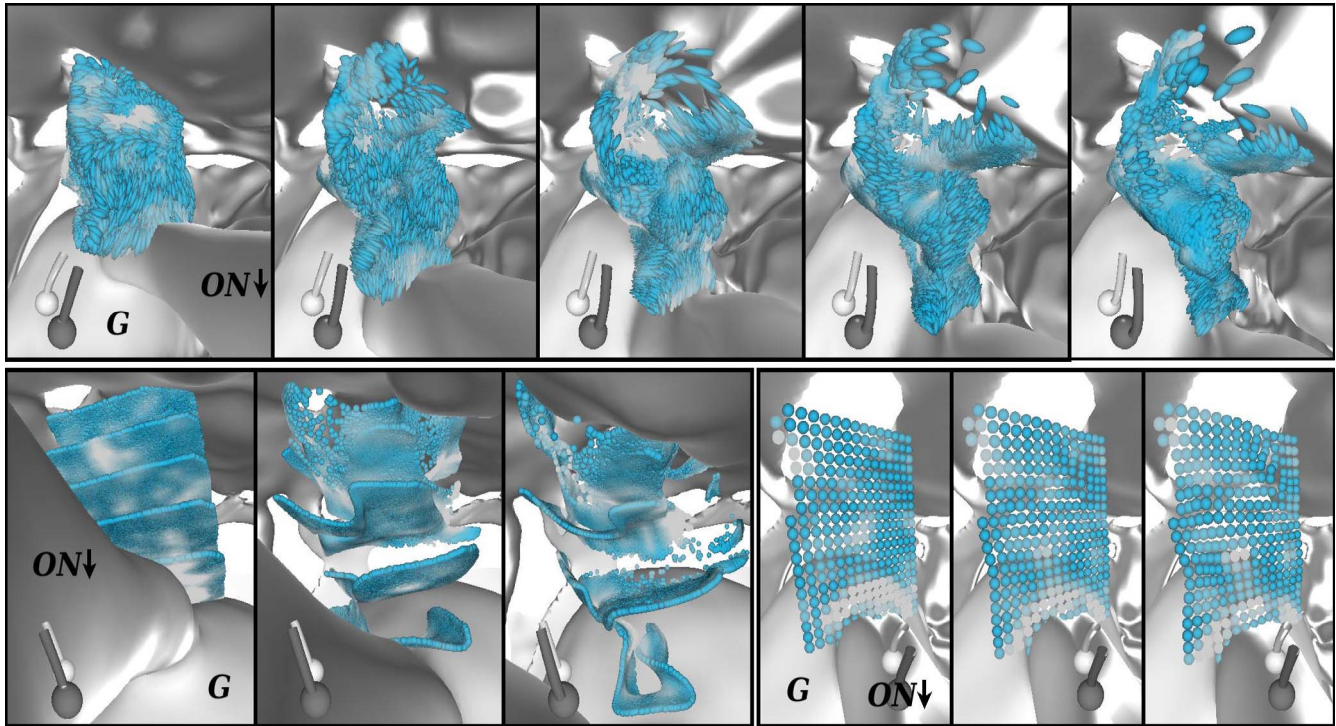
Figure 4. Marker seeding and deformation behind the optic nerve (B-splines). *Top panel*: random seeding inside a ROI just behind the optic nerve. Deformation is shown at approximately −30°, +5°, and +35° of eyeball rotation, respectively. The visualization shows stretching of the soft tissue volume right behind the optic nerve. *Bottom-left panel*: deformation visualized with a stack of six dense marker sheets, seeded at −30°. We see that the stack gets elongated and thinned in the optic nerve's direction of motion, as was apparent from the *left panel*. At +5°, the lowest sheet first shows that tissue not directly behind the optic nerve moves slower than tissue immediately behind it, as evidenced by the curling up of the sides of that marker sheet. At +35°, the invasion of sideways soft tissue in the ROI volume is indicated by the almost complete folding back onto itself of the sheet edges. *Bottom-right panel*: deformation of a single sheet of markers, seeded in a regular grid. Deformation is shown at approximately −30°, −27.5°, and −25°. When total deformation is small, the regular grid shows changes in marker positions that would not be clearly distinguishable in a randomly seeded ROI.

Figure 5 shows the ROI for sliding and deformation alongside the optic nerve. We expected to find that orbital fat moves less than the optic nerve and that this deformation decreases further with its distance to the optic nerve.[2] The deformation patterns near the apex of the orbit (bottom panels) show similar deformation on the inferior and superior sides of the optic nerve. Near the eyeball (top panels), the inferior side shows that tissue motion falls off proportionally to the distance to the optic nerve, up to a certain distance. On the superior side, the influence of the optic nerve on tissue motion seems more complicated. Less tissue seems to be dragged along with the optic nerve, while on the other hand, remaining tissue is pushed in the opposite direction, shown by the changing location of the approximately horizontal part of the marker sheet. Although the optic nerve is slightly closer to the superior rectus muscle than to the inferior rectus muscle, which could

explain the more limited range of influence in that direction, this does not explain the opposite motion of the fat on the superior side.

Displacement of Orbital Fat Between Eyeball and Medial and Lateral Rectus Muscles During Abduction

As mentioned earlier, we would expect orbital fat to be pushed out from between eyeball and muscle during eye rotation. During abduction, slight stretching of the marker configuration in axial direction is indeed observed in the area between the medial rectus muscle and the eyeball, indicating that the tissue is indeed squeezed from between the structures (Fig. 6, top). The amount of stretching, however, is not sufficient to fully support the muscle rolling up onto the eyeball, as a significant amount of fat appears to remain where the muscle would have displaced it. This is likely caused by lack of resolution in the MRI data and flaws in the deformation calculation method.
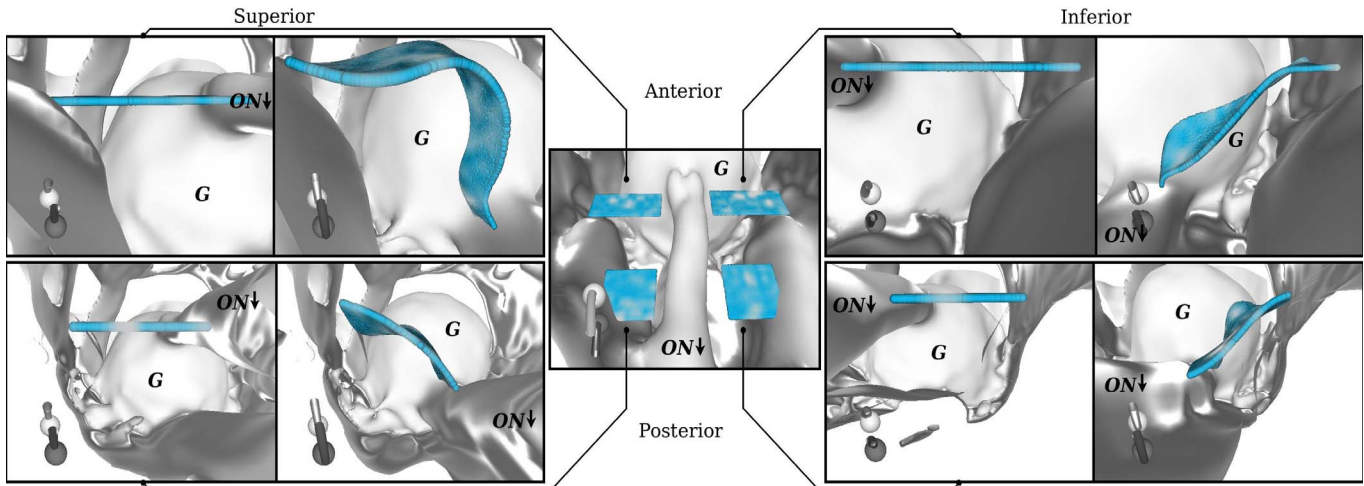
Figure 5. Deformation alongside the optic nerve (B-splines). Four panels, two images each, show orbital fat motion proportional to its distance to the optic nerve moving in the medial direction. Markers are seeded at −30° eyeball rotation, and are tracked until +40°. The *center image* provides an overview of where the marker sheets were seeded. *Top-left panel*: motion near the eyeball, superior side. There is a clear separation between fat that is moving with the optic nerve, and fat moving in the opposite direction, indicated by the steep slope of the originally horizontal right side, and the upward motion of the left part of the original marker sheet. *Top-right panel*: motion near the eyeball, inferior side. Fat deforms more gradually on the inferior side, and eventually is not influenced at all by the optic nerve motion. This is indicated by the gentler slope of the resulting marker sheet, and the immobility of the markers farthest away from the optic nerve. *Bottom-left and bottom-right panels*: motion near the orbit apex, superior and anterior sides, respectively. Because the optic nerve moves significantly less near the apex than near the eyeball, we see a similar pattern, but at a smaller scale. The opposite motion on the superior side, however, is largely absent, as is the longer range of influence of the optic nerve on the anterior side, resulting in fat deformation being more symmetrical near the orbit apex than near the eyeball.
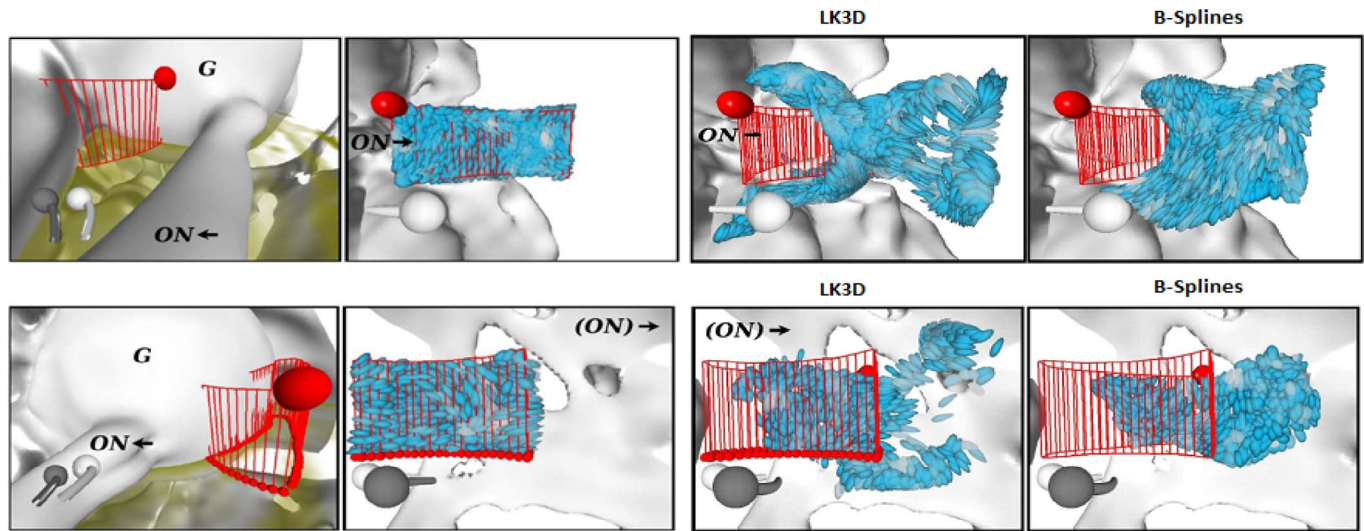
Figure 6. Deformation between eyeball and medial- (*top*) and lateral rectus muscle (*bottom*) during abduction. *Top-left*: ROI selection adjacent to the eyeball and medial rectus muscle, viewed from the orbit apex. *Center*: view of same ROI from within the eyeball, showing the initial marker configuration. *Top-right*: LK3D results are dominated by the approach of the optic nerve, shown by the vertical expulsion of markers only on the left, rather than the medial rectus muscle rolling up onto the eyeball. B-splines results for the same ROI again give the impression that the orbital soft tissue is more rubbery than fluid, judging from the little distortion and the lack of expected divergence. *Bottom-left*: ROI located adjacent to the eyeball and lateral rectus muscle. *Bottom-center*: View of same ROI from within the eyeball, showing the initial marker configuration. *Right*: LK3D results show generally correct direction of motion, although motion results are somewhat erratic. No significant compression of the volume in axial direction is observed. When using B-splines, the erratic behavior observed with LK3D is absent. Also B-splines shows the expected convergence of soft tissue as eye fat moves in from inferior and superior sides.
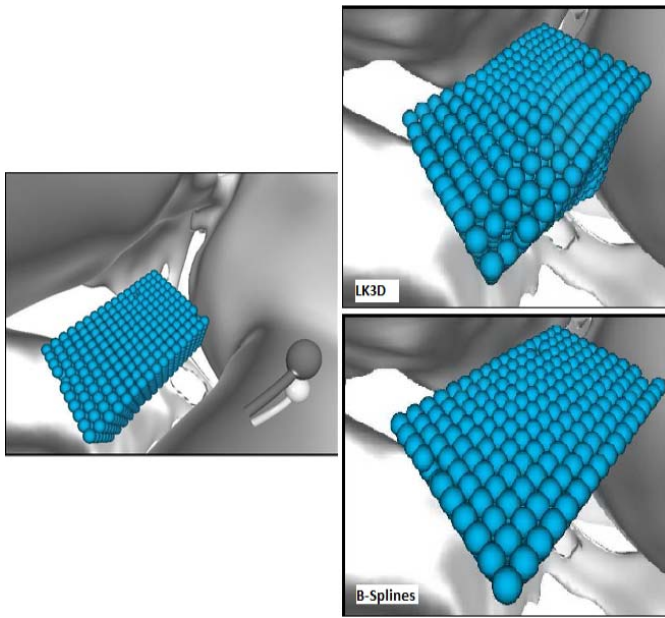
Figure 7. Deformation results for a uniformly translating MRI volume. *Left*: a regular grid of markers, seeded inside a box-shaped ROI. *Right*: deformation results after significant translation: B-splines results are close to being perfect as no distortion of the grid structure can be seen. LK3D results however, show a slight, but noticeable, deviation from the original grid structure.

When the eye abducts, we also expected to observe thinning of a marker volume in the axial direction between the eyeball and the lateral rectus muscle. Although we correctly see the fat rotating with the eyeball to some extent, the expected thinning is hardly observed (Fig. 6, bottom) as the resolution of the MRI images is insufficient.

Validation Experiments

As mentioned above, the first experiment involved a synthetic dataset, which was translating in a 3D space. As emphasized by the grid structure, the volume's shape and internal structure were indeed retained using the B-splines technique (Fig. 7).

When tracking the eye lens, the general direction of motion was correct. However, we observed some distortion of the original ROI shape using B-splines (Fig. 8) and even more using LK3D (Appendix B), while we know the ground truth to be the lens merely rotating with the eyeball in the axial plane without significantly changing its shape.

A similar result was witnessed when tracking a blood vessel section (Fig. 9). Using B-splines, the shape of the vessel remains intact as no disruption of tissue occurs.

Discussion

The role of the orbital fat in the mechanics of eye suspension and eye rotation has historically been greatly underappreciated while, in fact, it is of crucial importance. The four rectus muscles pull the eye backward and hold the eye, rolling and sliding on the
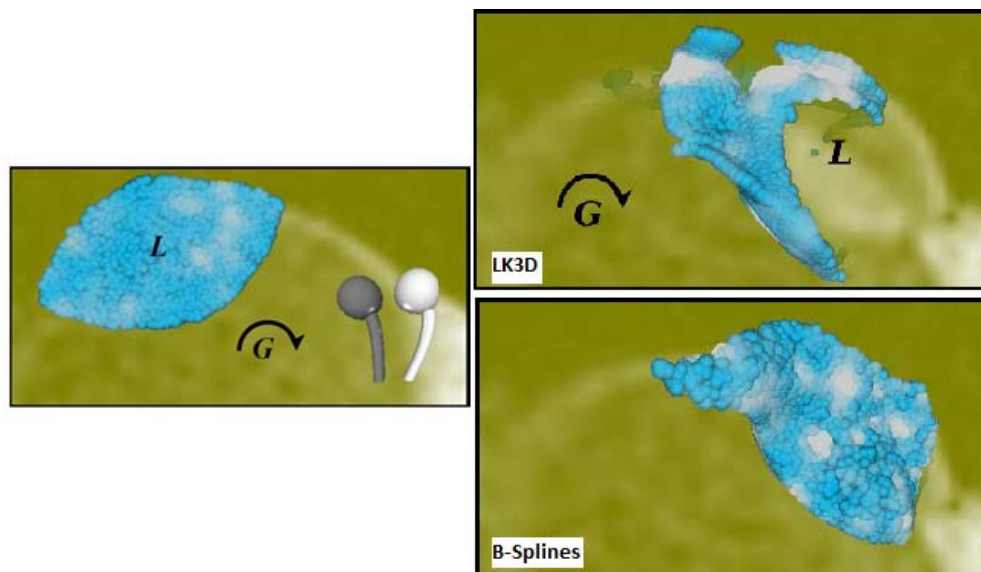
Figure 8. Deformation results for the lens. *Left*: axial view of the lens at −20° of eyeball rotation, showing markers that completely cover the lens. *Right*: results at +40. LK3D results show a lot of loss in the lens coverage. B-splines retains lens position and shape noticeably better than LK3D. The entire updated lens position remains covered in markers with B-splines, while most of it was bared with LK3D.
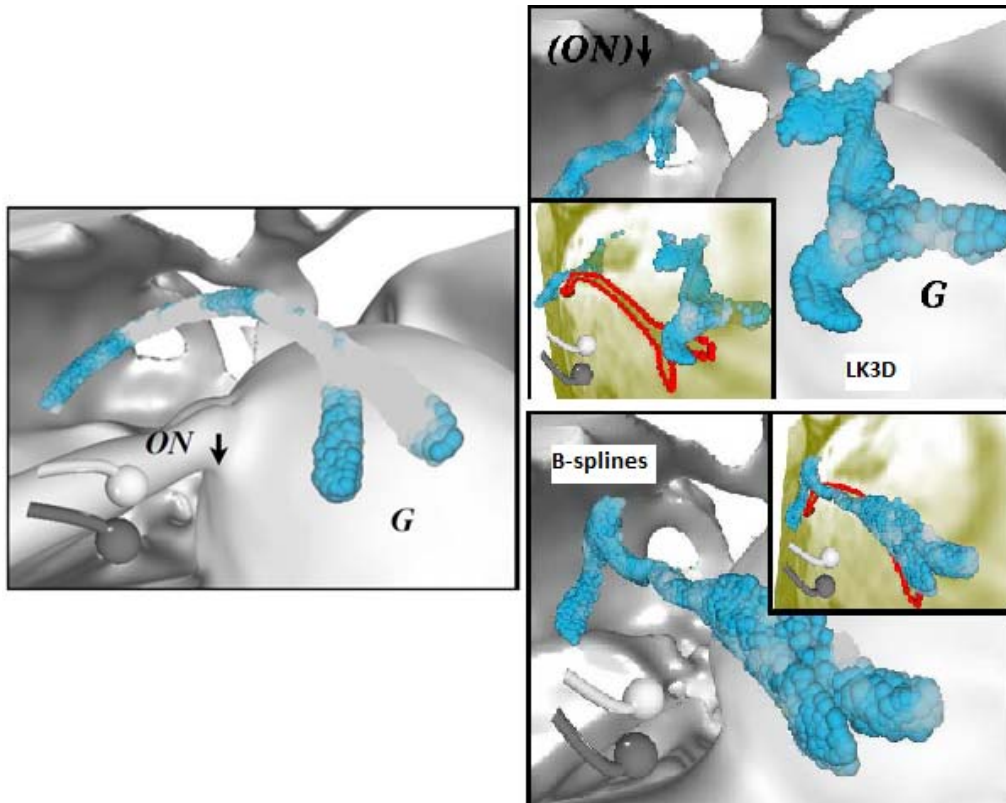
Figure 9. Deformation results for a blood vessel. *Left*: area around the blood vessel seeded with markers at −30° eyeball rotation. *Right*: deformation results at +35° for LK3D and B-splines. *Inset* shows in *red* the blood vessel's new location, according to the MRI data. LK3D results show the erroneous tearing of tissue. B-splines results for the same structure show that vein connectivity is preserved and the actual position of the vein is covered by more markers.

orbital fat. It could also be, in part, contributing to the pulley action of the eye muscles (i.e., the direction of pull of the eye muscles rotates with eye movement out of the plane of the muscle) as the rectus muscles are kept in place by the fat and its connective tissue.[18] Moreover, the sliding behavior of the orbital fat is essential for allowing high speed saccades (i.e., saccades would require more energy when the fat would be adherent to the eye and the eye muscles), and all the displacement were to be achieved by deformation. As the developed tool is able to visualize the sliding and deforming fat, it provides valuable information concerning the role of orbital fat in the mechanics of eye movement and suspension.

We compared two deformation calculation methods from a sequence of MRI volumes (LK3D and B-splines) in a pipeline for the visualization of orbital fat sliding and deformation during eye rotation and investigated which of the two is best suited to visualize three clinically relevant questions. Our comparison suggests that overall B-splines is the better choice. Mainly, B-splines shows less ripping of tissue such as

blood vessels and less distortion of structures such as the lens. On the other hand, however, because of the inability of B-splines to allow tissue to tear, it is unable to show the combination of sliding and extreme deformation, needed for the apparent disconnection of fat, as the optic nerve slides through it. This problem is not as apparent when using LK3D as it generates a more or less liquid behavior of the moving fat. So in fact, which calculation method is best suited depends on the actual situation: B-splines works better in tracking structures such as the lens, blood vessels, and parts of the fat, while LK3D allows tissue to disconnect as should happen as the optic nerve slides through the fat, or as an eye muscle rolls up onto the globe. This said, B-splines is available as a ready-to-use package where LK3D is not.

The difficulty of creating correct deformation calculation methods lies in the fact that different tissues slide along each other during eye rotation. As stated by Schmidt-Richberg et al.,[19] most techniques apply a certain smoothing condition to render a realistic representation. By doing so, it assumes that

the deformation occurs homogenously, and therefore loses accuracy when applied to different tissues sliding along each other. In their study, they have developed a technique to smooth the object and background separately and have applied it to the sliding behavior encountered in lung and liver motion during the respiration cycle.[19] Obviously, it would be of great interest to apply this technique to our data set. As mentioned before, deformation data can also be acquired in live tissue directly using 2D-tagged MRI[15–17,20] and the pipeline we discuss could be applied to a 3D version of tagged MRI. However, this technique is not accurate and fast enough in 3D.

We showed to what extent the orbital fat in the sclera-fat interface follows the movement of the eyeball during rotation. On this topic, a longstanding controversy exists. On one hand, the optic nerve cannot slosh through the fat when the eye rotates. On the other hand, however, complete rotation of orbital fat seems inefficient, as it would increase the momentum during eye rotation. In this study, we demonstrate that, in line with findings of Schoemaker et al.,[2] the fat immediately behind the eye follows eye movement by approximately one-half. Sliding of the eyeball over the retrobulbar fat must also be taken into account in future finite element models of the suspension of the eye in the orbit.[18]

Also, we found that the tissue regions in front of and behind the optic nerve seem to respectively be pushed away and to follow the optic nerve path in its wake, agreeing with results from Schoemaker et al. (Figs. 3 and 4).[2] Moreover, thin sheets in four areas alongside the optic nerve showed to what extent orbital fat at its side moves with the optic nerve as it slides through it, see Figure 5, also in line with results from the study of Schoemaker et al.[2] The fat around the optic nerve behaves almost like a fluid, whereas in other parts of the orbit, the fat is more firm, preventing for instance a sideways displacement of eye muscles through the fat.[21]

To what extent a particular volume of markers should deform as a lengthening rectus muscle rolls up onto the globe is unknown, because we have no ground truth with which to compare. However, the orbital fat between sclera and muscle is arranged in layers. Each layer is separated from adjacent layers by connective tissue sheets parallel tot sclera and muscle, permitting fast sideways extrusion of fat when the muscle rolls up onto the globe.[22] In line with this observation, we found that regions of orbital fat between the eyeball and the medial rectus muscle showed to some extent the expulsion of the fat as the

eye muscle rolls up onto the eyeball during abduction. However, fat moving in from above and below as the lateral rectus muscle rolls off from the eyeball could not be demonstrated, most likely due to a lack of resolution of the MRI images.

The aim of our present study was to describe the visualization technique in a single dataset. For further applicability it is imperative to analyze a sufficient number of orbital datasets. For the future, it would be interesting to adequately differentiate between sliding and deformation, as this further increases understanding of the fat's dynamic behavior. For instance, to what extent does an extraocular muscle slide over the orbital wall and in the back of the orbit? Furthermore, a principal component analysis of the deformation could quantify deformation properties such as shear, stress, rotation, and translation. This information could also be of value for future finite-element models of the orbit.

Also, the pipeline could be applied to other areas of fat and soft-tissue deformation in the human body, such as in the infrapatellar fat pad in the knee joint,[23] the adipose kidney capsule,[25] heart motion,[26] or blood flow,[26] and lungs. This can demonstrate the deformation visualization pipeline as a tool more generally applicable than to orbital fat deformation alone. Finally, as data quality improves, the value of our technique increases as its accuracy is bound only by the accuracy of the deformation data due to controllable marker granularity.

As for other imaging modalities, it would be interesting to see its applicability in ultrasound imaging. Rossi et al.[27] describe a technique of ultrasound image velocimetry using the robust image velocimetry (RIV) algorithm to quantify the vitreous velocity fields generated by saccades. In theory, the technique described in this paper could be applied to a 3D ultrasound dataset. B-splines, for example, have already been described in the segmentation of 3D echocardiography.[28] However, being a cavity filled solely with a gel-like structure, the pitfall of using a marker-based visualization technique for vitreous lies in the difficulty to specify a ROI in such a medium. After all, a ROI is necessary in dense 3D visualization to prevent visuals in irrelevant regions from occluding the currently more interesting parts of a 3D volume.

Our tool for orbital fat deformation and sliding, as outlined in this study, could offer the opportunity for orbital surgeons to, for example, accurately locate a region of cicatrization. Together with a finite-element model this could eventually assist in deciding to operate or not, improve surgical approach, permit an

individualized surgical plan, and reduce reoperation rates.

References

1. Bremond-Gignac D, Copin H, Cussenot O, Lassau JP, Henin D. Anatomical histological and mesoscopic study of the adipose tissue of the orbit. *Surg Radiol Anat*. 2004;26:297–302.
2. Schoemaker I, Hoefnagel PP, Mastenbroek TJ, et al. Elasticity, viscosity, and deformation of orbital fat. *Invest Ophthalmol Vis Sci*. 2006;47: 4819–4826.
3. Fleet D, Jepson A. Computation of component image velocity from local phase information. *Int J Comput Vision*. 1990;5:77–104.
4. Uras S, Girosi F, Verri A, Torre V. A computational approach to motion perception. *Biol Cybern*. 1988;60:79–87.
5. Singh A. Image-flow computation: an estimation-theoretic framework and a unified perspective. *CVGIP: Image Underst*. 1992;56:152–177.
6. Lucas BD, Kanade T. An iterative image registration technique with an application to stereo vision. *IJCAI*. 1981;121–130.
7. Abramoff MD, Niessen WJ, Viergever MA. Objective quantification of the motion of soft tissues in the orbit. *IEEE Trans Med Imaging*. 2000;19:986–995.
8. Abramoff MD, Viergever MA. Computation and visualization of three-dimensional soft tissue motion in the orbit. *IEEE Trans Med Imaging*. 2002;21:296–304.
9. Beauchemin SS, Barron JL. The computation of optical flow. *ACM Computing Surveys (CSUR)*. 1995;27:433.
10. Klein S, Staring M, Pluim JP. Evaluation of optimization methods for nonrigid medical image registration using mutual information and B-splines. *IEEE Trans Image Process*. 2007;16: 2879–2890.
11. Maintz JB, Viergever MA. A survey of medical image registration. *Med Image Anal*. 1998;2:1–36.
12. Dawant BM. Non-rigid registration of medical images: purpose and methods, a short survey. *Proc IEEE Int Symp Biomed Imag*. 2002:465–468.
13. Botha CP, Graaf T, Schutte S, et al. MRI-based visualisation of orbital fat deformation during eye motion. In: Linsen L, Hagen H, Hamann B, eds. *Visualization in Medicine and Life Sciences*. Heidelberg, Germany: Springer; 2008:221–233.
14. Busking S, Botha CP, Post FH. Direct visualization of deformation in volumes. *Computer Graphics Forum*. 2009;28:799–806.
15. Piccirelli M, Luechinger R, Rutz AK, Boesiger P, Bergamin O. Extraocular muscle deformation assessed by motion-encoded MRI during eye movement in healthy subjects. *J Vis*. 2007;7(5): 1–10.
16. Piccirelli M, Luechinger R, Sturm V, Boesiger P, Landau K, Bergamin O. Local deformation of extraocular muscles during eye movement. *Invest Ophthalmol Vis Sci*. 2009;50:5189–5196.
17. Prince JL, McVeigh ER. Motion estimation from tagged MR image sequences. *IEEE Trans Med Imaging*. 1992;11:238–249.
18. Schutte S, van den Bedem SP, van Keulen F, van der Helm FC, Simonsz HJ. A finite-element analysis model of orbital biomechanics. *Vision Res*. 2006;46:1724–1731.
19. Schmidt-Richberg A, Werner R, Handels H, Ehrhardt J. Estimation of slipping organ motion by registration with direction-dependent regularization. *Med Image Anal*. 2012;16:150–159.
20. Piccirelli M, Bergamin O, Landau K, Boesiger P, Luechinger R. Vitreous deformation during eye movement. *NMR Biomed*. 2012;25:59–66.
21. van den Bedem SP, Schutte S, van der Helm FC, Simonsz HJ. Mechanical properties and functional importance of pulley bands or 'faisseaux tendineux'. *Vision Res*. 2005;45:2710–2714.
22. Koornneef L. New insights in the human orbital connective tissue. Result of a new anatomical approach. *Arch Ophthalmol*. 1977;95:1269–1273.
23. Hoffa AA. The influence of the adipose tissue with regard to the pathology of the knee joint. *J Am Med Assoc*. 1904;XLIII:795–796.
24. Lim JH, Kim B, Auh YH. Anatomical communications of the perirenal space. *Br J Radiol*. 1998; 71:450–456.
25. Holland AE, Goldfarb JW, Edelman RR. Diaphragmatic and cardiac motion during suspended

breathing: preliminary experience and implications for breath-hold MR imaging. *Radiology*. 1998;209:483–489.

26. Routh HF. Preliminary studies into high velocity transverse blood flow measurement. In: Pusateri TL, Waters DD, eds. *Ultrasonics Symposium Proceedings*. Piscataway: IEEE; 1990:1523–1526.

27. Rossi T, Querzoli G, Pasqualitto G, et al. Ultrasound imaging velocimetry of the human vitreous. *Exp Eye Res*. 2012;99:98–104.

28. Barbosa D, Dietenbeck T, Heyde B, et al. Fast and fully automatic 3-d echocardiographic segmentation using B-spline explicit active surfaces: feasibility study and validation in a clinical setting. *Ultrasound Med Biol*. 2013;39:89–101.

translational vision science & technology